Ultrafast Nonlinear Plasmon Decay Processes in Silver Nanoclusters

Gowri U. Kuda-Singappulige[a], David B. Lingerfelt[b,c], Xiaosong Li[b] & Christine M. Aikens[a,*]

[a]Department of Chemistry, Kansas State University, Manhattan, KS 66506, USA

[b]Department of Chemistry, University of Washington, Seattle, WA 98195, USA

[c]Center for Nanophase Materials Sciences, Oak Ridge National Laboratory, Oak Ridge, TN 37831, USA

*cmaikens@ksu.edu, 1-785-532-0954, fax: 1-785-532-6666

ABSTRACT

Tunable plasmonic properties of metallic nanostructures play a significant role in enhancing various photo-optical phenomena including solar energy conversion, nonlinear optics, photoluminescence and photocatalysis. Understanding the fast plasmon decay mechanisms is essential for developing practical applications utilizing these light-matter interaction processes, but has been a challenge both experimentally and computationally. Among theoretical simulation methods, real-time density functional theory (RT-TDDFT) is a valuable tool to monitor the electron dynamics of molecules subjected to an electric field. Herein, we use the RT-TDDFT method to identify the possible plasmon decay mechanisms of the bare tetrahedral Ag_8 nanocluster. We excite the strong linear plasmonic states and examine dipole response and the electron dynamics in the system. Variation of density matrix elements related to occupied and virtual orbital pairs reveals that the one-photon allowed transitions, which have been excited due to the incident electric field, experience ultrafast decay into high energy transitions, specifically to two-photon allowed transitions. The tetrahedral symmetry representations of these transitions confirm that some of these high energy transitions are only allowed via two-photon absorption whereas others can be activated via both one- and two- photon absorption. Moreover, this work suggests that the collective excitations present in the system play an important role in accumulating an enormous amount of energy to enhance nonlinear processes. Overall, this work provides insights into a possible plasmon decay mechanism of nanoclusters which is activation of nonlinear processes such as two-photon absorption.

INTRODUCTION

In the presence of electromagnetic radiation, the conduction electrons of noble metal nanoparticles oscillate with a resonant frequency with respect to the nanoparticle core; this phenomenon is known as a localized surface plasmon resonance and results in a strong peak in the optical absorption/extinction spectrum. The frequency and the strength of the oscillation depends on the size, shape and the composition of the nanoparticles.[1-3] Plasmonic features of noble metal nanoparticles including strong absorption of UV/visible and near-infrared (near-IR) portions of the electromagnetic spectrum lead to their use in solar cells,[4-6] bio-medical applications,[7-10] nonlinear optical convertors,[11-17] etc. However, the plasmon resonance decays quickly over time when the irradiation is turned off. Since applications typically benefit from slower damping, there is growing research interest in understanding the possible plasmon decay mechanisms. Excited electrons can slowly decay radiatively into photons[18] and this process is well-understood because they have nanosecond decay times and can be studied experimentally using time-resolved measurements.[3, 19] Faster electron scattering and non-radiative decay pathways, however, have been a subject of debate in recent literature. The electronic dephasing of metal nanoparticles occurs at a fast rate, which is typically within a few tens to hundreds of femtoseconds.[20-22] Therefore, it is experimentally challenging to capture the mechanisms involved in the ultrafast plasmon resonance dynamics. Theoretical computations help understand these fast-electronic processes and ultimately provide a pathway to manipulate the plasmonic properties of nanoparticles. Classical electrodynamic methods such as Mie theory[23] and discrete dipole approximation (DDA)[24] can be successfully applied to simulate the optical response of large nanoparticles (diameter > 10 nm).[25]

However, they do not explicitly treat electrons and are unable to examine processes such as electron-electron scattering and other quantum effects.[26-27]

Time-dependent density functional theory (TDDFT), especially real-time time-dependent density functional theory (RT-TDDFT),[28-29] is a powerful tool to monitor fast electron dynamics. This method is currently available in a variety of codes[29-33] and provides optical absorption spectra that are consistent with the results from conventional linear response time-dependent density functional theory (LR-TDDFT) for diverse systems in a weak field.[34-35] A recent review on RT-TDDFT has been provided by Goings et al.[36] Due to its computational efficiency for large systems as well as its applicability in the nonlinear regime, RT-TDDFT is beneficial for exploring plasmonic properties and electron dynamics of metal nanoparticles.[37-41] Nevertheless, the RT method often lacks information about the origin of the excitations that is naturally generated by the LR method. Several studies, however, show that this information can be resolved. Ding et al.[40] analyzed the time evolution of molecular orbital occupation numbers and demonstrated that collective and in-phase oscillations of single-particle transitions are associated with the transverse plasmon excitations of silver nanowires. Moreover, the variation of the off-diagonal elements of the density matrix corresponding to a pair of occupied and unoccupied orbitals provides a straightforward picture of the time variation of electronic transitions.[42-45] Repisky and co-workers first proposed the dipole-weighted matrix analysis to interpret the molecular orbital transitions corresponding to the spectral energies.[42-43] Bruner et al. introduced a Padé approximation to accelerate the transform of the individual contributions into the frequency domain and demonstrated its efficiency on gas phase water and a nickel porphyrin system.[44] Rossi et al. recently used this concept to present a benchmark study on small benzene derivatives followed by application to icosahedral silver nanoparticles consisting of 55 to 561 atoms.[45] Sinha-Roy et al.

showed the ability to accurately extract transition densities of the excited states from a single δ-kick RT-TDDFT calculation.[46]

The above-mentioned studies were generally limited to static spectral properties rather than the time evolution of plasmons. One exception is a recent theoretical study in which Ma and coworkers[38] suggested that the plasmon resonance of the Ag_{55} cluster decays into single particle excitations that can be identified as hot carriers. In addition, real-time electron dynamics simulations done by Rossi et al.[47] have also identified the plasmon dephasing into hot carriers in large silver nanoparticles. In a recent theoretical study, Yan et al.[48] showed that the hot carriers generated by plasmon decay in silver atomic chains lead to nonlinear effects. It is clear that plasmon induced nonlinear processes including second harmonic generation have become a hot topic in the photonics field.[49-55] However, a clear understanding of plasmon decay mechanisms has not yet been achieved; to fully understand plasmon decay mechanisms, the fast electron dynamics of nanoparticles upon irradiation with light must be further studied within a quantum mechanical framework. In this work, we investigate the electron dynamics of a tetrahedral Ag_8 cluster with RT-TDDFT simulations to explore its fast plasmon decay mechanisms.

COMPUTATIONAL DETAILS

The electron dynamics of the Ag_8 (T_d) cluster was studied using RT-TDDFT in a development version of the Gaussian software.[56] The BP86[57-58] exchange-correlation functional with the LanL2DZ[59-61] effective core potential basis set were used for all calculations. Geometry optimization calculations were carried out followed by TDDFT calculations on the optimized structures (coordinates provided in the SI). The highly symmetric T_d isomer of the Ag_8 cluster has been previously observed to be the global minimum structure (Figure 1, inset).[62] We first compared the optical absorption properties of Ag_8 obtained from both LR-TDDFT and RT-TDDFT. In the LR calculations, 800 electronic excitations were calculated to obtain the optical absorption energies up to around 9 eV. A Gaussian broadening with a full width at half maximum (FWHM) of 0.2 eV was used when plotting absorption spectra with LR-TDDFT to account for the experimental vibrational broadening at room temperature. To determine the spectral properties from RT-TDDFT, the electron density is converged to self-consistency in the presence of a step function external field applied along the z axis with an amplitude of 0.001 a.u. (~3.57×10^{13} W/cm^2). In this manner, all electronic states are excited simultaneously. Then, the density is propagated for 120 fs with a time step of 0.0012 fs. The time-dependent dipole moment is related to the absorption cross section by Fourier transformation into the frequency domain.[28, 36] An exponential damping corresponding to a Lorentzian spectral line shape ($1/\Gamma$ = 855 a.u. of time) was added to the time dependent dipole moment ($D'(t) = D(t)exp^{-\pi\Gamma t}$, where $D(t)$ is the observed dipole moment and $D'(t)$ is the damped dipole moment) before Fourier transformation, which gives a broadening similar to our LR-TDDFT calculations.

To explore the plasmon decay mechanisms, we study the electron dynamics of the Ag_8 cluster subjected to a trapezoidal-shaped electric field along the z axis using RT-TDDFT. The field is gradually increased to its highest amplitude of 0.001 a.u. (~3.57×10^{13} W/cm^2) over the time period from 0 to 1 fs. The field is then applied continuously at a constant amplitude and a constant frequency until 19 fs when the amplitude function starts to decrease, and is completely turned off at 20 fs (Figure S1a). The gradual increase and decrease avoid artifacts that can arise from a sudden application of a continuous wave field. In this way, one can study the electron dynamics of a system excited by a quasi-monochromatic laser, which we will refer to as a continuous wave throughout the text, applied for a certain period of time. The variation of the dipole moment of Ag_8 resulting from the applied field is shown in Figure S1b. The Fourier transform of a field applied with a frequency corresponding to 3.96 eV confirms that the excitation is indeed centered around 3.96 eV (Figure S1c). In this work, the frequencies that are resonant with the lowest two excitation energies of the Ag_8 cluster, as determined by LR-TDDFT, are used as the frequencies of the applied electric fields. The electron density is allowed to propagate for a total time of 240 fs with a 0.002 fs step size and the dipole response was inspected.

Numerical propagation of the time-dependent Kohn-Sham equation is used to determine the electron dynamics via the time-dependent density matrix in the molecular orbital basis.[63-64] The time-dependent Kohn-Sham equation in an orthonormal basis is given in eq 1, where $P(t)$ is the time-dependent density matrix in the orthonormal basis, $K(t)$ (eq 2) is the time-dependent Kohn-Sham matrix under the influence of an external electric field $E(t)$, and $K_0(t)$ is the unperturbed Kohn-Sham matrix.

$$i\frac{dP(t)}{dt} = [K(t), P(t)] \quad (1)$$

$$K(t) = K_0(t) - \mu \cdot E(t) \tag{2}$$

The Kohn-Sham matrix in its eigenspace is written as:

$$C^{\dagger}(t_n) \cdot K(t_n) \cdot C(t_n) = \varepsilon(t_n) \tag{3}$$

where $C(t_n)$ and $\varepsilon(t_n)$ are the eigenvectors and eigenvalues of the perturbed Kohn-Sham matrix respectively. The electron density is propagated using the modified mid-point unitary transformation algorithm (MMUT).[63, 65] In this formalism the unitary transformation matrix *U* at time t_n is calculated as follows where Δt is the time step:

$$U(t_n) = exp\big(i\Delta t K(t_n)\big) = C(t_n) \cdot exp\big(i\Delta t \varepsilon(t_n)\big) \cdot C^{\dagger}(t_n) \tag{4}$$

The density matrix at time t_{n-1} is then propagated to time t_{n+1} using $U(t_n)$ (eq 5).

$$P(t_{n+1}) = U(t_n) \cdot P(t_{n-1}) \cdot U^{\dagger}(t_n) \tag{5}$$

At each time step, the time-varying density matrix is also transformed into the eigenbasis of the initial perturbation-free Kohn Sham matrix (i.e., the canonical molecular orbital basis) according to eq 6, with $C_0^{\dagger} \cdot K_0(t_0) \cdot C_0 = \varepsilon_0(t_0)$. P_{MO} refers to the density matrix in the molecular orbital basis. We examine the variation of off-diagonal elements of the density matrix P_{OV}, corresponding to pairs of occupied (O) and virtual (V) molecular orbitals, to track the contributions from each occupied-to-virtual molecular orbital pairs to the total electron dynamics. The Fourier analysis of P_{OV} identifies the frequency of its oscillation. Exploring these time-varying off-diagonal elements of the MO-based density matrix after exciting a single electronic state is our unique approach to discover the possible electronic transitions that emerge as a result of the plasmon decay.

$$P_{MO}(t) = C_0^{\dagger} \cdot P(t) \cdot C_0 \tag{6}$$

RESULTS AND DISCUSSION

Electronic structure and absorption properties of Ag_8

An orbital energy level diagram of the tetrahedral Ag_8 cluster illustrating the primary orbitals that are involved in the electronic transitions is shown in Figure 1. In addition to the standard orbital designations under tetrahedral symmetry, the orbitals are also labeled with their closest spherical superatomic[66] molecular orbital notation. In superatomic nomenclature,[66] capital letters such as S and P are used to represent molecular orbitals that are delocalized throughout the entire nanocluster; the letters S and P indicate that these molecular orbitals have the same nodal symmetry as the spherical harmonics representing *s* and *p* atomic orbitals. Then, the electronic configuration arising from eight 5*s* valence electrons of silver atoms can be designated as $1S^2 1P^6$. As shown in Figure 1, the 1S orbital (45) with a_1 symmetry lies very low in energy compared to the frontier orbitals. The HOMO level is triply degenerate corresponding to a 1P-like set of orbitals (74-76) with t_2 symmetry. An additional set of molecular orbitals that are mostly localized on the silver atoms and arise from linear combinations of atomic 4d orbitals lies between the 1S and 1P levels; this set of orbitals is denoted as the d-band. The specific T_d point group symmetry representations of these d-band orbitals are shown in Figure 1. The 1D-type virtual orbitals (77-79, 81-82) are split into two sets with t_2 and e symmetry due to the tetrahedral geometry of the cluster. The superatomic 2S orbital (80) with a_1 symmetry lies between the two sets of 1D orbitals. Above these orbitals, the degenerate 2P orbitals (83-85) lie higher in energy followed by 1F-type orbitals (87-92); the triply degenerate 2P orbitals have t_2 symmetry and the 1F orbitals split into three sets with a_1, t_1 and t_2 representations in the tetrahedral environment. The HOMO-LUMO gap of the tetrahedral Ag_8 cluster is found to be 2.31 eV at the BP86/LanL2DZ level of theory.

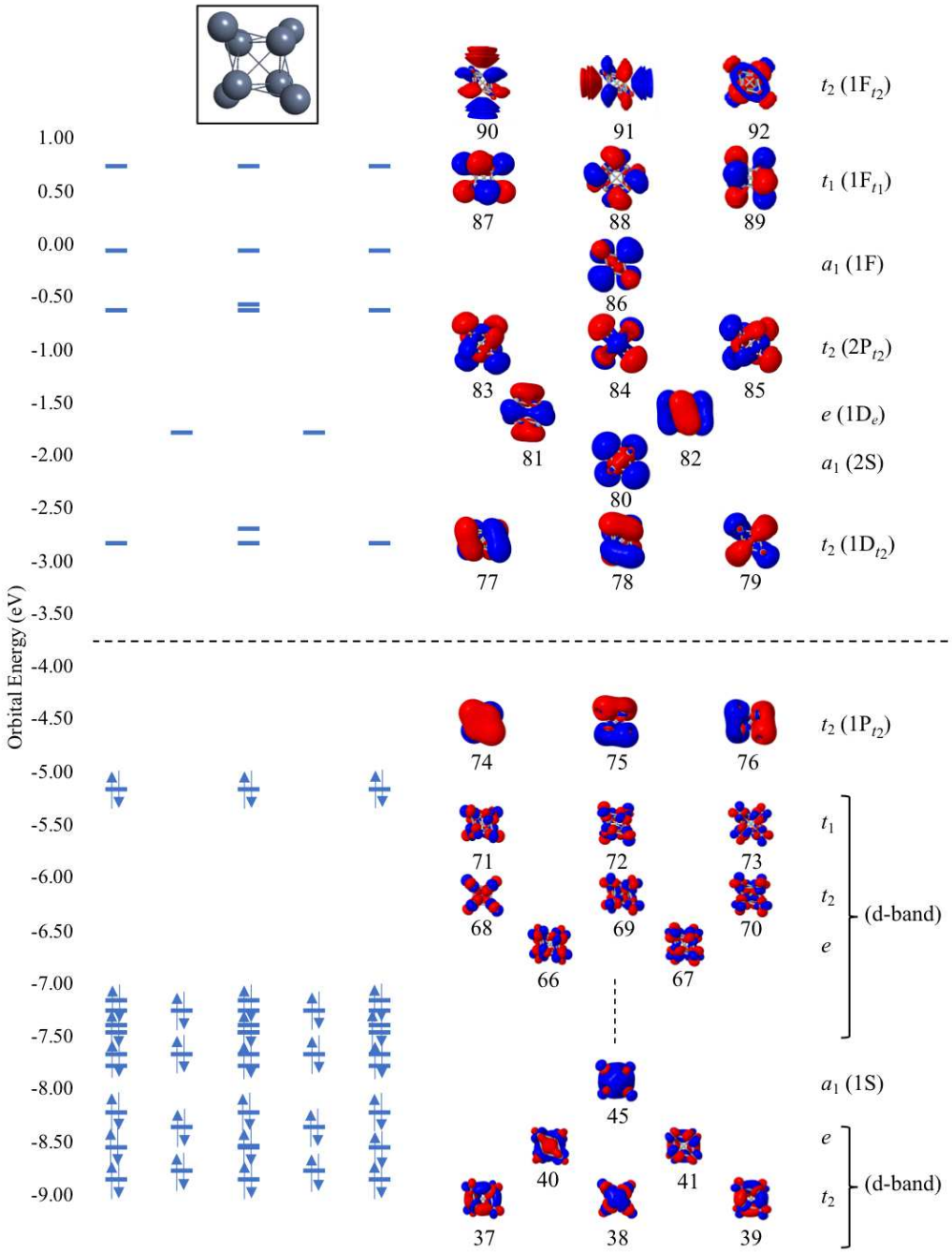

Figure 1. Molecular structure and the orbital energy level diagram of the tetrahedral Ag_8 cluster. Shapes and the tetrahedral point group symmetry representations of the orbitals are displayed with

the relevant spherical assignment for the superatomic orbitals in parentheses. A horizontal dashed line separates the occupied and virtual orbitals.

The absorption spectrum of the Ag_8 tetrahedron contains two sharp peaks at 3.05 eV and 3.96 eV as calculated from linear-response TDDFT (Figure 2). The peak at 3.05 eV arises due to electronic transitions from the occupied 1P orbitals into the unoccupied 1D and 2S orbitals (Table S1). For the excitation at 3.96 eV, the largest contribution comes from 1P → 1D transitions, although some 1P → 2S and d-band → 1D transitions also contribute slightly (Table S2). The electronic transitions between superatomic orbitals of Ag_8 follow the spherical selection rule, $\Delta L = \pm 1$, for these lowest two excitations. Moreover, these transitions follow the specific selection rules for dipole-allowed electronic transitions in a molecule with T_d point group symmetry. The absorption spectrum calculated from the RT-TDDFT calculation, i.e. the Fourier-transformed dipole moment, reproduces the spectrum calculated from LR-TDDFT (Figure S2). Molecular orbital occupation number variation and their Fourier transforms (Figure S3) as well as the Fourier analysis of the off-diagonal density matrix elements (Figure S4) support the spectral transition information revealed by LR-TDDFT. Most importantly, since these excitations arise due to the constructive contribution of multiple electronic transitions, we can identify that they correspond to a molecular analog of a plasmon resonance in this nanocluster; thus, the electronic dynamics in this nanocluster provide important information about possible plasmon decay mechanisms.

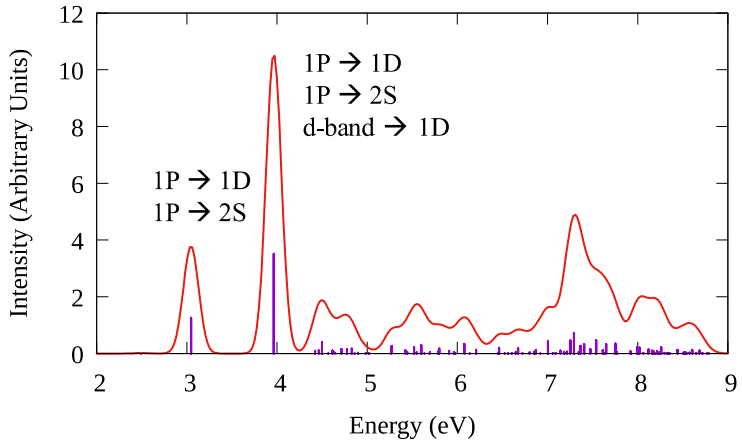

Figure 2. LR-TDDFT excitation spectrum of the tetrahedral Ag_8 cluster and the transitions responsible for the peaks at 3.05 eV and 3.96 eV. (Purple: LR stick spectrum; red: convoluted spectrum using gaussian curves with Gaussian FWHM = 0.2 eV).

Real-time TDDFT of Ag_8 with a continuous wave field

To study the plasmon dynamics of this system, continuous wave external electric fields with resonant frequencies of 3.05 eV and 3.96 eV are applied and the dipole moment variations over time are examined. We first focus on the most intense peak, which appears at 3.96 eV. The time variation of the applied field oscillating with a frequency corresponding to 3.96 eV is shown in Figure 3a. (An expanded view from 0 fs to 20 fs is shown in Figure S1a; its corresponding Fourier transform in Figure S1c confirms that the pulse will excite electronic states centered around 3.96 eV.) The dipole moment of the silver cluster subjected to this continuous wave field is shown in Figure 3b. Due to the continuous energy supplied during the first 20 fs, the dipole moment resonating with the applied field frequency continues to increase until the field is turned off at 20 fs (Figures 3b and S1b). After the external field is turned off, the dipole moment starts to decrease but continues to oscillate at the resonant frequency. The magnitude of the dipole moment continues to drop until about 175 fs when it again starts to rise. This behavior of the dipole moment

implies that the collective (dipolar plasmon-like) behavior in the Ag_8 cluster is decaying between 20 and 175 fs. However, it should be noted that in our simulation the total energy is conserved and the nuclei are fixed; thus, energy cannot flow into vibrational modes. In the absence of any energy dissipation processes, the energy arising from the interaction of the nanoparticle with the electric field will stay in electronic states for the entire length of the simulation, although it may flow between different electronic states due to coherences established in the system during the electric field perturbation. In a "real" system, this energy will decay to nuclear degrees of freedom (typically on the time scale of 100s of fs) and then to the bath (1000s of fs). Thus, although we would expect beating if we were to run the simulation in this paper for many hundreds or thousands of fs, this would not truly simulate what may occur experimentally. We are most interested in the short-time decay dynamics of the electronic states. Therefore, the question arises of where the energy flows when the dipolar oscillation decreases during the initial dipolar decay.

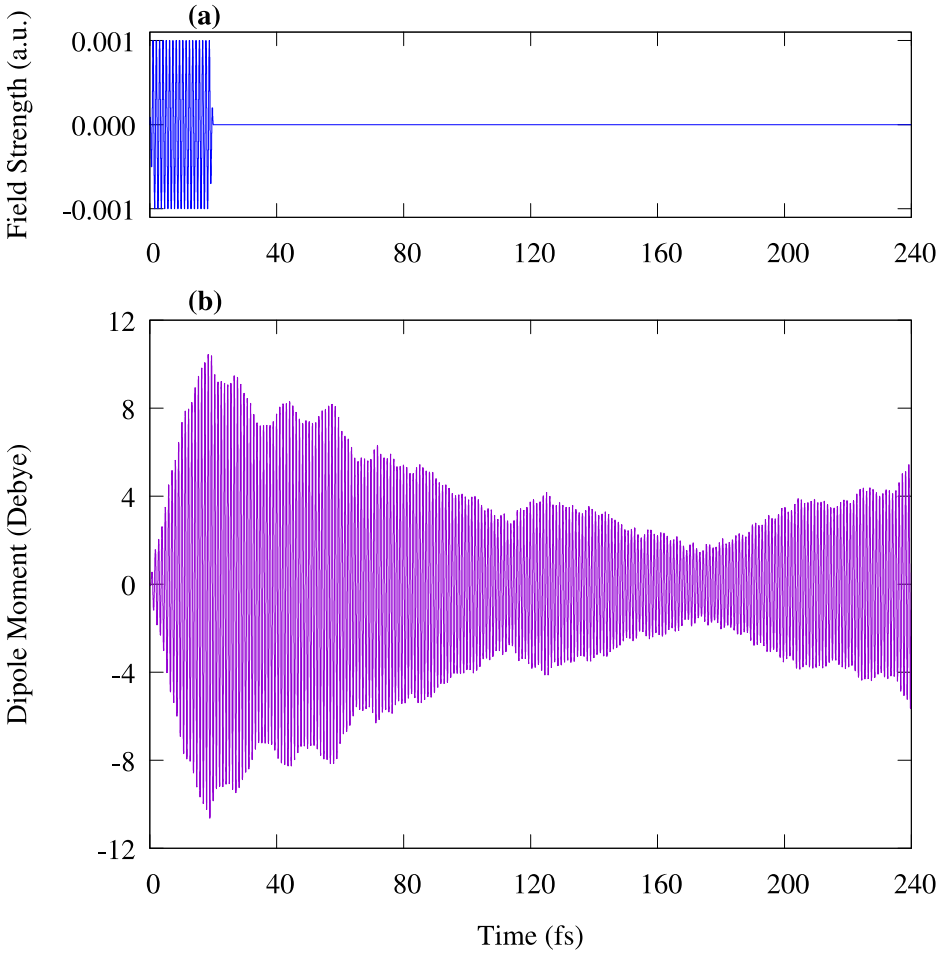

Figure 3. Variation of (a) applied electric field and (b) dipole moment along z axis. The continuous wave electric field is applied with a frequency of 3.96 eV.

To identify the energy transfer over the course of the electron dynamics simulation, we analyze the variation of the off-diagonal density matrix elements, P_{OV}, corresponding to occupied-virtual molecular orbital pairs. The value of P_{OV} at a certain time indicates the amount of single particle electronic transition occurring between the occupied and the virtual orbital at that time. Variation of the P_{OV} element corresponding to a transition between an occupied 1P-type molecular orbital (75) and a virtual 1D-type orbital (81) (Figure 4a) follows the same temporal pattern as the dipole moment variation, where the transition is the strongest around 20 fs and decays to a

minimum near 175 fs. Similar variations albeit with smaller magnitudes are observed for the 1P → 2S (Figure 4b) and d-band → 1D transitions (Figure S5d). The corresponding Fourier transforms in Figure 4c indicate that these transitions are related to the activation of the plasmonic excitation at 3.96 eV. Further analysis of the orbital occupation variation in individual orbitals shows that the electron population of occupied orbital 75 decays until 20 fs and starts to grow after 20 fs, whereas the population of virtual orbital 81 shows an anticorrelation with that of occupied orbital 75 (Figure S6, middle), demonstrating that the dynamics of this electron transition as measured by orbital occupation numbers are similar to the dynamics manifested by $P_{75\text{-}81}$. The continuous drop of $P_{75\text{-}81}$ even after 60 fs through about 175 fs is clearly shown in the variation of corresponding orbital occupations. Here we note that when we excite the system with a continuous wave electric field corresponding to a resonant energy of the molecule, the frequency domain dipole response as well as the molecular orbital responses slightly shift towards higher energy. For instance, when an energy of 3.96 eV is applied to the system as a continuous wave electric field, the frequency domain responses for both the dipole moment and the off-diagonal density matrix elements peak at 4.03 eV. The shift in the time dependent response in RT-TDDFT where the system is perturbed significantly away from the ground state has been previously reported by several researchers.[67-70] In this work, the amount of this observed peak shifting was less than 0.1 eV and can be considered to be very small.

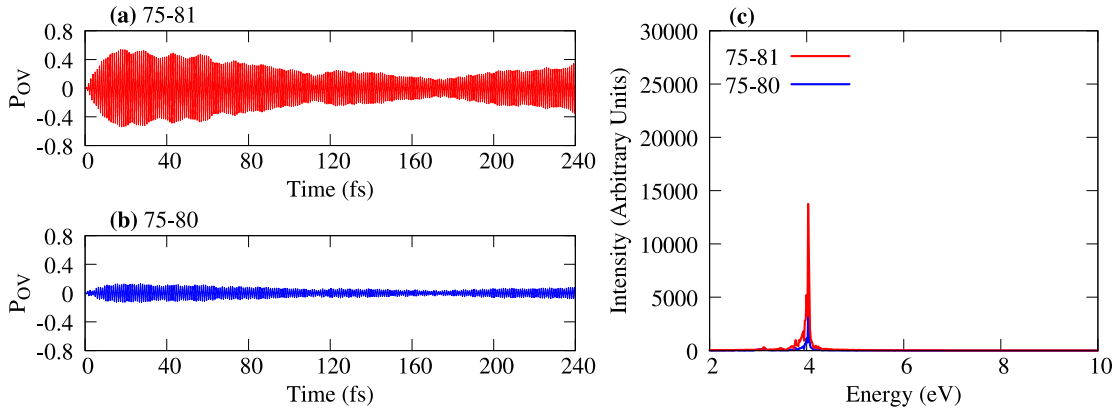

Figure 4. Variation of density matrix elements corresponding to the occupied and virtual pairs (a) 1P – 1D and (b) 1P – 2S; (c) corresponding Fourier transforms. The continuous wave electric field is applied with a frequency of 3.96 eV.

Overall, variation of 1P → 1D, 1P → 2S and d-band → 1D transitions follow the same pattern as the dipole moment variation oscillating with the resonant frequency; these transitions were also identified from the linear response calculations described above as the transitions responsible for the collective plasmon-like peak at 3.96 eV. Point group symmetries indicate that these 1P → 1D, 1P → 2S and d-band → 1D transitions are electric dipole-allowed, owing to the fact that the irreducible representations of the corresponding direct products contain the T_2 representation (Table 1). Density matrix element variations corresponding to the dipole-allowed transitions separated into their point group representations are presented in Figure S5.

Table 1. Tetrahedral point group representations of the orbitals involved in the transitions which give rise to the peaks at 4.03 eV and 8.07 eV and the decomposition of their direct products. Note: The continuous wave electric field is applied with a frequency of 3.96 eV.

Excitation energy (eV)	**Transitions**	**Spherical assignments**	**Symmetry**	**Direct product decomposition into irreducible representation**

4.03	75 → 81 74 → 81	1P → 1D	$t_2 \rightarrow e$	$T_1 + T_2$
	76 → 77	1P → 1D	$t_2 \rightarrow t_2$	$A_1 + E + T_1 + T_2$
	75 → 80	1P → 2S	$t_2 \rightarrow a_1$	T_2
	66 → 78 66 → 79	d-band → 1D	$e \rightarrow t_2$	$T_1 + T_2$
8.07	45 → 86	1S → 1F	$a_1 \rightarrow a_1$	A_1
	72 → 92 71 → 90 73 → 90	d-band → 1F	$t_1 \rightarrow t_2$	$A_2 + E + T_1 + T_2$
	68 → 90 69 → 91 69 → 92 70 → 91 70 → 92	d-band → 1F	$t_2 \rightarrow t_2$	$A_1 + E + T_1 + T_2$

Because the time-dependent behavior of the dipole-allowed transitions resembles the variation of the dipole moment, these transitions do not reveal any new information regarding the energy transfer processes that are active during the 20-175 fs time period. However, several other transitions were found to behave in a different manner. Interestingly, the P_{OV} matrix element corresponding to the 45 (1S) → 86 (1F) transition grows significantly even after the field is switched off at 20 fs (Figure 5a). The oscillation of this transition corresponds to an energy of 8.07 eV (Figure 5b), which is twice the resonant frequency. In addition to this transition between two superatomic orbitals, some d-band transitions also gain energy and oscillate with a frequency corresponding to 8.07 eV (Figure 5b, c). A summary of transitions oscillating with 8.07 eV frequency is illustrated in Figure S7. As compared in Figure 6, the decay of $P_{75\text{-}81}$ (1P → 1D transition) and growth of $P_{45\text{-}86}$ (1S → 1F transition) are related. The density matrix element $P_{75\text{-}81}$ starts to increase right away as the field is applied and keeps increasing until the field is turned off at 20 fs. In contrast, $P_{45\text{-}86}$ starts to increase at around 5 fs and continues to grow even after 20 fs

(Figure 6). Anticorrelated dynamics of occupation numbers for orbitals 45 (occupied) and 86 (virtual) underscore the electron transition dynamics occurring between these two orbitals (Figure S6, bottom). The inverse correlation between the two types of transitions (1P → 1D with 1ω, where ω is 3.96 eV, and 1S → 1F with 2ω), especially after the field is turned off, suggests that the energy flows from the dipole-allowed transitions into different transitions with twice the plasmon energy. Similarly, around 175 fs the electron occupation in orbital 75 (1P) reaches a maximum at essentially 2 electrons, while the occupation of 81 (1D) drops back to 0 electrons (Figure S6, middle). This corresponds to the time at which the dipole moment of the system reaches a minimum. At the same time, the electron occupation of orbital 45 (1S) reaches a minimum (~1.75 electrons) while the occupation of orbital 86 (1F) reaches a maximum (~0.25 electrons) (Figure S6, bottom). The magnitude of the dipole moment as well as the P_{OV} elements corresponding to dipole-allowed transitions start to increase after about 175 fs (Figure 3b and Figure 6). This might suggest that the dipole-allowed transition could undergo a revival at some time. Comparatively, P_{OV} elements related to the two-photon allowed transitions drop after 175 fs (Figure S7). This illustrates why a permanent decay of the dipole moment may not be possible under the adiabatic conditions used in these simulations. In reality, however, a revival back to the initial states may

not actually occur. At longer time scales, energy transfer to vibrational energy may play a role in addition to energy transfer to the bath.

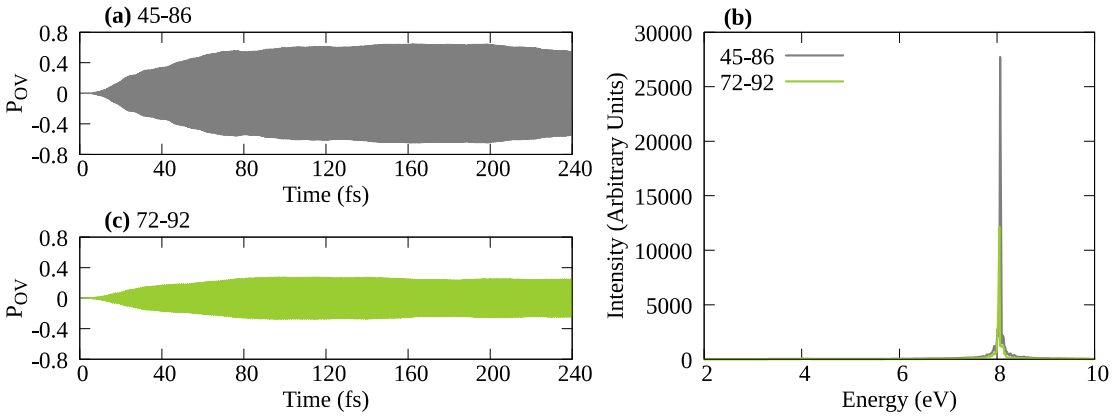

Figure 5. Variation of density matrix elements corresponding to the occupied and virtual pairs (a) 1S – 1F (45-86) and (c) d-band – 1F (72-92); (b) corresponding Fourier transforms. The continuous wave electric field is applied with a frequency of 3.96 eV.

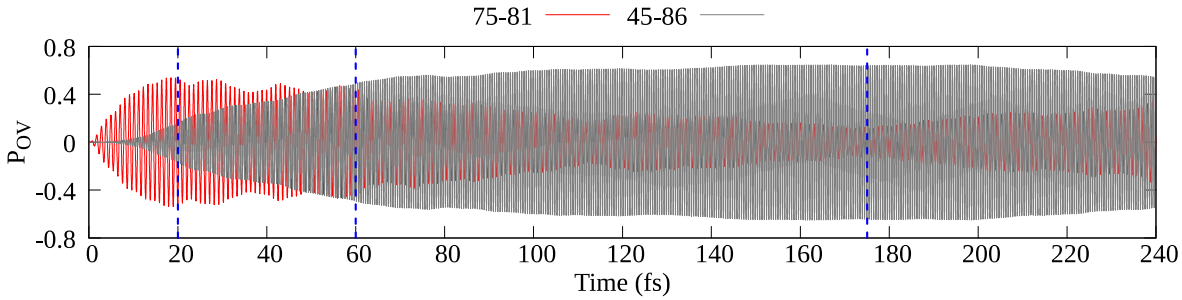

Figure 6. Decay of $P_{75\text{-}81}$ and growth of $P_{45\text{-}86}$ when the continuous wave electric field is applied with a frequency of 3.96 eV.

The energy of the continuous wave field is clearly centered around the energy corresponding to the applied frequency without significant excitation at higher energies (Figure S1b), even though the continuous wave field is only applied for 20 fs. Therefore, the non-linear

effects arise as a result of the electron dynamics in the nanocluster, not because of direct excitation arising from the short-time application of the continuous wave field.

When a system is excited with a resonant electric field, excitation of the dipole-allowed transitions is expected. However, here we not only observe these one-photon excitations but also numerous two-photon absorptions due to the presence of a strong electric field. The selection rules for allowed two-photon absorption are analogous to the selection rules for Raman scattering.[71-74] Therefore, for a two-photon absorption to be allowed, the direct product of the representations of the initial and final molecular orbitals corresponding to an electronic state should contain a quadratic representation such as xy, yz, x^2, y^2, etc. Referring to the character table of the T_d point group, if the direct product of symmetries of the two orbitals involved in a transition includes A_1, E or T_2, then that transition can be allowed for two-photon absorption. As shown in Table 1, 1S → 1F and d-band → 1F transitions, which give rise to the excitation at 8.07 eV, are in fact two-photon allowed. Importantly, we observe that the transition between superatomic 1S and 1F orbitals, which is of A_1 symmetry, is forbidden for one-photon absorption but allowed with two-photon excitation. Therefore, the applied field is strong enough to create nonlinear effects resulting in this excitation with A_1 symmetry. Additionally, in a tetrahedral molecule, which does not have a center of inversion, there can be transitions that are both one- and two-photon allowed. The transitions between d-band (t_1/t_2) and 1F (t_2) orbitals can be both one- and two-photon allowed because the direct products $t_1 \otimes t_2$ and $t_2 \otimes t_2$ yield T_2 symmetry.

We also reduced the strength of the electric field by a factor of 10 and identified the same behavior albeit with decreased magnitudes for the dipole moment and density matrix elements. The comparison of the dipole moment variation and the corresponding Fourier transforms for the

applied field strengths 0.001 a.u. and 0.0001 a.u. are presented in Figure S8. Figure S9 and Figure S10 illustrate the variation of density matrix elements and their Fourier transforms corresponding to one- and two-photon allowed transitions respectively. The dipole moment as well as the P_{OV} values of one-photon allowed transitions decrease by a factor of 3-7 while the P_{OV} values of two-photon allowed transitions decreases by a factor of 17-19 when the electric field is weaker by a factor of 10. Although this decrease is not at the maximum factor of 100 that could be expected for a second-order nonlinear process, it is larger than the factor of 10 that would be expected for a purely linear process, thereby implicating nonlinear processes. Dipole decay occurs more rapidly for the stronger applied field, which correlates with the observation that the two-photon allowed transitions are activated more during the simulation with the stronger field. It is possible in larger plasmonic nanoparticles that the very strong near-fields created by the collective oscillation of the conduction electrons upon resonant excitation even with a low-intensity laser are sufficient to induce plasmon decay via two-photon processes; this should be the topic of a future study.

We likewise examined the electron dynamics of Ag_8 excited at the resonant energy of 3.05 eV. Similar to the previous results, the dipole moment along the z axis (Figure 7b) is dominated by the 1P → 1D and 1P → 2S transitions (Figure 8a,b) that make up the excitation at 3.05 eV, consistent with LR-TDDFT findings. The magnitudes of the corresponding P_{OV} elements and the dipole moment increase until the field is turned off and start to decay after that. These transitions again start to grow at about 80 fs. Over the 240-fs simulation, we observe these transitions and dipole moments fall and rise several times indicating energy transfer to and from other transitions. The corresponding Fourier transforms show a peak at around 3.07 eV (Figure 8c), confirming their contribution to the resonant peak (note that the system was excited with a continuous wave electric field oscillating with a frequency of 3.05 eV and we observe a peak shifting of 0.02 eV here).

There are three types of transitions, $t_2 \rightarrow e$, $t_2 \rightarrow t_2$ and $t_2 \rightarrow a_1$, that follow the dipole moment signature and all of them yield the T_2 representation (Table 2 and Figure S11). Therefore, they are dipole-allowed according to the T_d point group symmetry rules. Here also we perceive the activation of two-photon excitations. Figure 8d,e illustrates the variation of P_{OV} for the transitions from low-lying d orbitals to 2S and 1D orbitals oscillating with twice the resonant frequency, i.e. 6.19 eV (Figure 8f, Table 2, Figure S12). As shown in Table 2, the symmetries of these transitions follow the selection rules for two-photon absorption because their direct products include the A_1, E or T_2 representations. The inter-band transition of d electrons to the 2S level is the major two-photon transition when the system is initially excited at 3.05 eV. Because this transition has E symmetry, it requires a strong field to be activated via multiple photons. Similar to the previous discussion, these d-band transitions do not occur as soon as the field is applied but start to increase their strength at around 5 fs. This clearly implies the ultrafast decay of one-photon excitations into two-photon excitations.

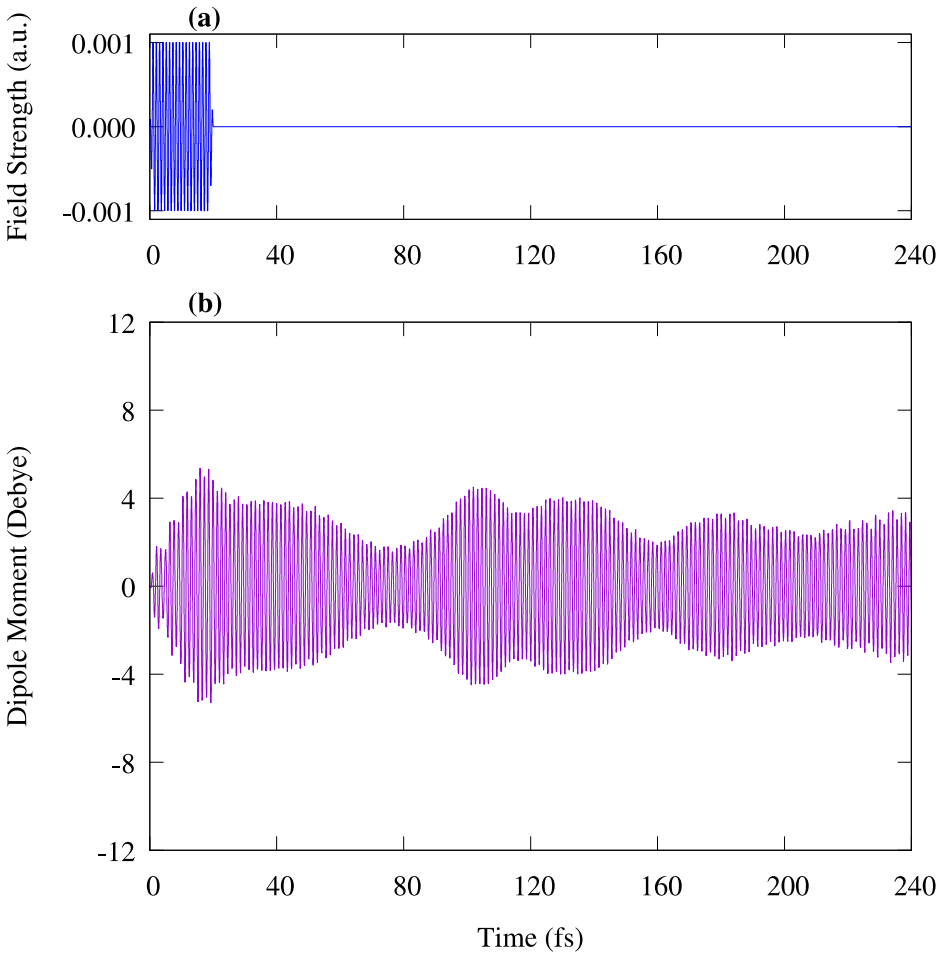
(a)
Field Strength (a.u.)
0.001
0.000
-0.001
0
40
80
120
160
200
240
(b)
Dipole Moment (Debye)
12
8
4
0
-4
-8
-12
0
40
80
120
160
200
240
Time (fs)

Figure 7. Variation of (a) applied electric field and (b) dipole moment along z axis. The continuous wave electric field is applied with a frequency of 3.05 eV.

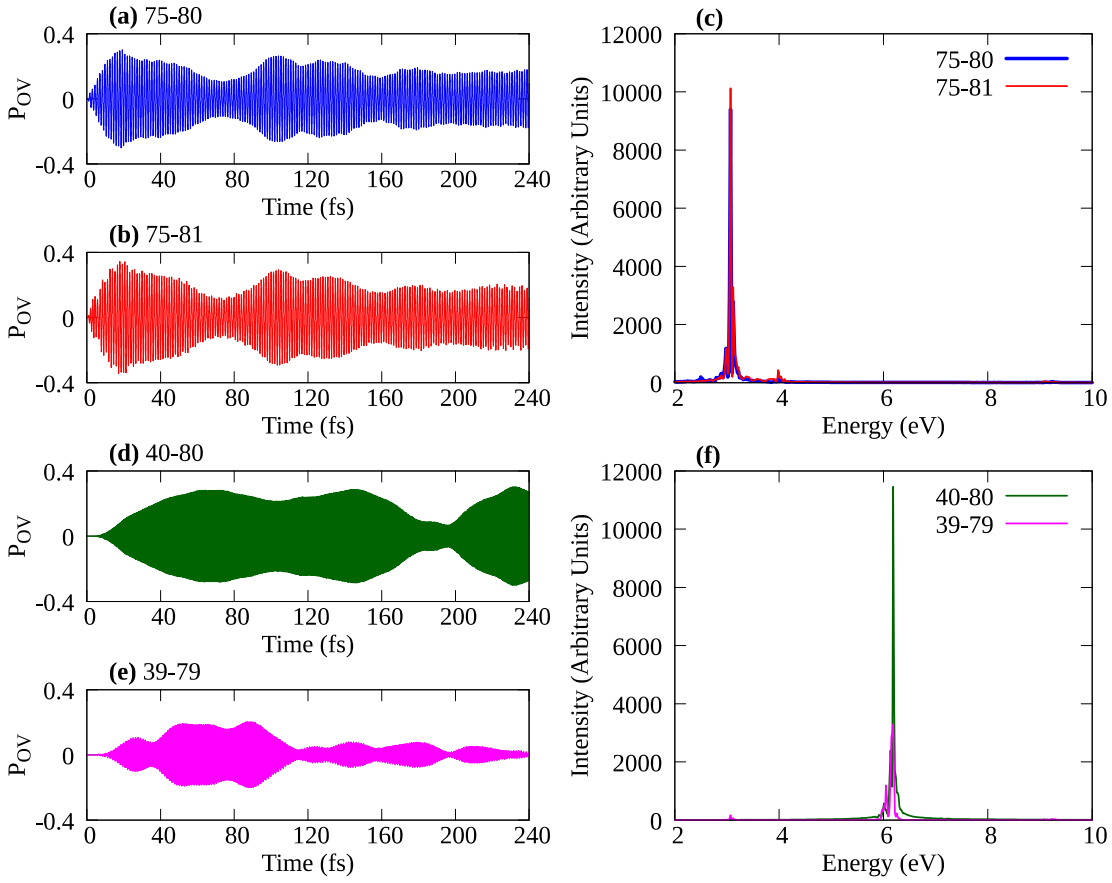

Figure 8. Variation of P_{OV} corresponding to (a) 1P → 2S, (b) 1P → 1D transitions and (c) corresponding Fourier transforms; variation of (d) d-band → 2S, (e) d-band → 1D transitions and (f) corresponding Fourier transforms. The continuous wave electric field is applied with a frequency of 3.05 eV.

Table 2. Tetrahedral point group representations of the orbitals involving in the transitions that give rise to the peaks at to 3.07 eV and 6.19 eV and the decomposition of their direct products. Note: The continuous wave electric field is applied with a frequency of 3.05 eV.

Excitation energy (eV)	**Transitions**	**Spherical assignments**	**Symmetry**	**Direct product decomposition into irreducible representation**
3.07	74 → 81 75 → 81 76 → 81	1P → 1D	$t_2 \rightarrow e$	$T_1 + T_2$
	74 → 79 76 → 77 74 → 78 75 → 77 75 → 79 76 → 78	1P → 1D	$t_2 \rightarrow t_2$	$A_1 + E + T_1 + T_2$
	74 → 80 75 → 80 76 → 80	1P → 2S	$t_2 \rightarrow a_1$	T_2
6.19	40 → 80	d-band → 2S	$e \rightarrow a_1$	E
	38 → 78 37 → 77 39 → 79	d-band → 1D	$t_2 \rightarrow t_2$	$A_1 + E + T_1 + T_2$
	45 → 80	1S → 2S	$a_1 \rightarrow a_1$	A_1

In both cases where the system is excited by a continuous wave electric field (with energies of 3.05 eV and 3.96 eV), the collective plasmon resonance of this tetrahedral Ag_8 cluster decays

into high-energy excited states with twice the resonant energy, resembling the two-photon absorption phenomenon. The electric field intensity of 0.001 a.u. (~3.57×10^{13} W/cm^2) is strong enough to induce nonlinear effects of this tetrahedral cluster, and weaker nonlinear processes are also observed for the applied electric field with an intensity of 0.0001 a.u. Tetrahedral symmetry may play an important role in allowing these two-photon absorption processes because there are states that could be accessible via both one- and two-photon absorption. Nonetheless, the strongest contributions to the high-energy two-photon absorptions around 6.19 eV and 8.07 eV arise from transitions with E and A_1 symmetry, respectively, which are prohibited in the linear regime. Overall, the role of shape and symmetry in enabling nonlinear absorption processes in nanoclusters will be a valuable area for further study.

In the tetrahedral Ag_8 cluster, the two lowest excited states at 3.05 eV and 3.96 eV have T_2 symmetry leading to the possibility that each of these plasmon-like states can also be activated via two photon-absorption if they are excited with a frequency corresponding to half of the resonant excited state energy. To test this possibility, we applied continuous wave electric fields with energies of 1.525 eV and 1.98 eV (corresponding to half of the energy of the strong, collective states at 3.05 eV and 3.96 eV) using electric field intensities of 0.001 a.u. However, we observed neither a continuous increment of the dipole moment while the field is applied, nor two-photon absorption for these frequencies. Variation of the applied field, dipole moment and the Fourier transformed dipole moment compared with the LR peak positions for these two frequencies are shown in Figures S13 and S14. In both cases, the time variation of the dipole moment resembles that of the applied field rather than an increasing dipole moment while the field is applied. The magnitude of the dipole moment in both cases is around 1 Debye, which is weaker compared to the corresponding dipole moment when excited at a plasmonic frequency (i.e. 10 Debye and 5

Debye when excited with resonant frequencies of 3.96 eV and 3.05 eV, respectively). After 20 fs, the dipole moment oscillates with either of the two lowest plasmonic frequencies. Surprisingly, when excited with a continuous electric field oscillating with an energy of 1.525 eV, after 20 fs the dipole response oscillates with a frequency corresponding to 3.96 eV excitation rather than with 3.05 eV, which would have been twice the applied frequency. Furthermore, the 1.98 eV excitation leads to an oscillation of the dipole moment with a frequency corresponding to a peak at 3.05 eV instead of one at 3.96 eV which would be expected if nonlinear processes were occurring in this situation. This remarkable observation suggests that even in the presence of a strong field, two-photon absorption may not occur for all incident wavelengths of light, regardless of whether the corresponding two-photon excitations are allowed. However, wavelengths corresponding to resonant excitations such as plasmon resonances can significantly enhance the possibility of two-photon absorption. Plasmonic systems can absorb a massive amount of energy when excited at plasmon resonance frequency and can use that energy to initiate multi-photon processes. Therefore, plasmonicity appears to be a driving force for the activation of nonlinear absorption properties.

SUMMARY

Herein we demonstrate a possible plasmon-enhancement of nonlinear susceptibility in the tetrahedral Ag_8 cluster. Electron dynamics in this silver cluster subjected to a continuous wave electric field oscillating at two plasmonic resonance frequencies were examined using RT-TDDFT. We observe an ultrafast decay of the dipolar response after the external field is turned off, especially when the strongly dipole-allowed plasmon-like state is excited. The unique approach used in this work, the analysis of the time-dependent off-diagonal density matrix elements in the MO basis, reveals that the dominant transitions that govern the resonant plasmonic state decay in the absence of the electric field, whereas the density matrix elements related to several other MO transitions continue to rise. Surprisingly, these growing matrix elements oscillate at twice the incident frequency demonstrating a strong second-order nonlinear response. This work shows that the dipole-allowed one-photon excitations can be transformed into two-photon allowed states in this tetrahedral cluster which can be considered a plasmon-mediated nonlinear response. The distinct point group symmetry selection rules for one- and two-photon absorption confirm the linear and nonlinear transitions respectively. This work also reveals the fact that the incident electric field must be in resonance with strong collective excited states such as plasmon resonances to substantially boost the nonlinear properties. This work establishes an interesting area of research, i.e. ultrafast plasmon decay via nonlinear processes, for future understanding of energy enhancement and transfer processes in plasmonic materials.

SUPPORTING INFORMATION AVAILABLE

Coordinates of Ag_8 cluster. Applied continuous wave field and the dipole moment of the Ag_8 cluster in both time and energy domains. Transitions responsible for the lowest energy peaks of the Ag_8 cluster at 3.05 eV and 3.96 eV. Absorption spectra comparison for LR and RT-TDDFT methods. Analysis of spectral properties from the molecular orbital occupation number variation and off-diagonal elements of the density matrix during time propagation. Decay and growth of off-diagonal density matrix elements when external continuous wave electric fields oscillating with frequencies of 3.96 eV and 3.05 eV are applied. Variation of the occupation numbers for selected molecular orbitals (3.96 eV excitation). Comparison of the dipole response and the P_{OV} values when the applied field strengths are 0.001 a.u. and 0.0001 a.u. Variation of applied field, dipole moment along z axis and Fourier transformed dipole moment when continuous wave electric fields oscillating with frequencies of 1.525 eV and 1.98 eV are applied.

ACKNOWLEDGMENTS

This material is based on work supported by the Department of Energy under grant DE-SC0012273. The computing for this project was performed on the Beocat Research Cluster at Kansas State University, which is funded in part by NSF grants CHE-1726332, CNS-1006860, EPS-1006860, and EPS-0919443. The development of the first-principles electronic dynamics is supported by the U.S. Department of Energy (DE-SC0006863 to X.L.). The development of the linear-response TDDFT method for computational spectroscopy was supported by the National Science Foundation (CHE-1856210 to X.L.).

REFERENCES

1. Wang, W.; Yu, P.; Zhong, Z.; Tong, X.; Liu, T.; Li, Y.; Ashalley, E.; Chen, H.; Wu, J.; Wang, Z. Size-Dependent Longitudinal Plasmon Resonance Wavelength and Extraordinary Scattering Properties of Au Nanobipyramids. *Nanotechnology* **2018**, *29*, 355402/1-8.

2. Zhang, Q.; Ge, J.; Goebl, J.; Hu, Y.; Sun, Y.; Yin, Y. Tailored Synthesis of Superparamagnetic Gold Nanoshells with Tunable Optical Properties. *Adv. Mater.* **2010**, *22*, 1905-1909.

3. Giannini, V.; Fernández-Domínguez, A. I.; Heck, S. C.; Maier, S. A. Plasmonic Nanoantennas: Fundamentals and Their Use in Controlling the Radiative Properties of Nanoemitters. *Chem. Rev.* **2011**, *111*, 3888-3912.

4. Xiao, M.; Jiang, R.; Wang, F.; Fang, C.; Wang, J.; Yu, J. C. Plasmon-Enhanced Chemical Reactions. *J. Mater. Chem. A* **2013**, *1*, 5790-5805.

5. Ueno, K.; Oshikiri, T.; Sun, Q.; Shi, X.; Misawa, H. Solid-State Plasmonic Solar Cells. *Chem. Rev.* **2018**, *118*, 2955-2993.

6. Zhang, Y.; He, S.; Guo, W.; Hu, Y.; Huang, J.; Mulcahy, J. R.; Wei, W. D. Surface-Plasmon-Driven Hot Electron Photochemistry. *Chem. Rev.* **2018**, *118*, 2927-2954.

7. Barizuddin, S.; Bok, S.; Gangopadhyay, S. Plasmonic Sensors for Disease Detection - A Review. *J. Nanomed. Nanotechnol.* **2016**, *7*, 373-373.

8. Elahi, N.; Kamali, M.; Baghersad, M. H. Recent Biomedical Applications of Gold Nanoparticles: A Review. *Talanta* **2018**, *184*, 537-556.

9. Kailasa, S. K.; Koduru, J. R.; Desai, M. L.; Park, T. J.; Singhal, R. K.; Basu, H. Recent Progress on Surface Chemistry of Plasmonic Metal Nanoparticles for Colorimetric Assay of Drugs in Pharmaceutical and Biological Samples. *Trends Anal. Chem.* **2018**, *105*, 106-120.

10. Zhang, Z.; Wang, H.; Chen, Z.; Wang, X.; Choo, J.; Chen, L. Plasmonic Colorimetric Sensors Based on Etching and Growth of Noble Metal Nanoparticles: Strategies and Applications. *Biosens. Bioelectron.* **2018**, *114*, 52-65.

11. Genevet, P.; Tetienne, J.-P.; Gatzogiannis, E.; Blanchard, R.; Kats, M. A.; Scully, M. O.; Capasso, F. Large Enhancement of Nonlinear Optical Phenomena by Plasmonic Nanocavity Gratings. *Nano Lett.* **2010**, *10*, 4880-4883.

12. Schuller, J. A.; Barnard, E. S.; Cai, W.; Jun, Y. C.; White, J. S.; Brongersma, M. L. Plasmonics for Extreme Light Concentration and Manipulation. *Nat. Mater.* **2010**, *9*, 193-204.
13. Grubisic, A.; Ringe, E.; Cobley, C. M.; Xia, Y.; Marks, L. D.; Van Duyne, R. P.; Nesbitt, D. J. Plasmonic Near-Electric Field Enhancement Effects in Ultrafast Photoelectron Emission: Correlated Spatial and Laser Polarization Microscopy Studies of Individual Ag Nanocubes. *Nano Lett.* **2012**, *12*, 4823-4829.
14. Kauranen, M.; Zayats, A. V. Nonlinear Plasmonics. *Nat. Photonics* **2012**, *6*, 737-748.
15. Panoiu, N. C.; Sha, W. E. I.; Lei, D. Y.; Li, G. C. Nonlinear Optics in Plasmonic Nanostructures. *J. Opt.* **2018**, *20*, 083001.
16. Sivis, M.; Pazos-Perez, N.; Yu, R.; Alvarez-Puebla, R.; García de Abajo, F. J.; Ropers, C. Continuous-Wave Multiphoton Photoemission from Plasmonic Nanostars. *Commun. Phys.* **2018**, *1*, 13.
17. Yu, H.; Peng, Y.; Yang, Y.; Li, Z.-Y. Plasmon-Enhanced Light–Matter Interactions and Applications. *Npj Comput. Mater.* **2019**, *5*, 45.
18. Maier, S. A. *Plasmonics: Fundamentals and Applications*; Springer, New York, NY, 2007.
19. Kretschmann, E.; Raether, H. Radiative Decay of Non Radiative Surface Plasmons Excited by Light. *Z. Naturforsch. A* **1968**, *23*, 2135-2136.
20. Liau, Y.-H.; Unterreiner, A. N.; Chang, Q.; Scherer, N. F. Ultrafast Dephasing of Single Nanoparticles Studied by Two-Pulse Second-Order Interferometry. *J. Phys. Chem. B* **2001**, *105*, 2135-2142.
21. Sönnichsen, C.; Franzl, T.; Wilk, T.; von Plessen, G.; Feldmann, J.; Wilson, O.; Mulvaney, P. Drastic Reduction of Plasmon Damping in Gold Nanorods. *Phys. Rev. Lett.* **2002**, *88*, 077402/1-4.
22. Lazzarini, C. M.; Tadzio, L.; Fitzgerald, J. M.; Sánchez-Gil, J. A.; Giannini, V. Linear Ultrafast Dynamics of Plasmon and Magnetic Resonances in Nanoparticles. *Phys. Rev. B* **2017**, *96*, 235407/1-11.
23. Mie, G. Beiträge zur Optik trüber Medien, speziell kolloidaler Metallösungen. *Ann. Phys. (Berl.)* **1908**, *330*, 377-445.

24. Draine, B. T.; Flatau, P. J. Discrete-Dipole Approximation For Scattering Calculations. *J. Opt. Soc. Am. A* **1994**, *11*, 1491-1499.

25. Zhao, J.; Pinchuk, A. O.; McMahon, J. M.; Li, S.; Ausman, L. K.; Atkinson, A. L.; Schatz, G. C. Methods for Describing the Electromagnetic Properties of Silver and Gold Nanoparticles. *Acc. Chem. Res.* **2008**, *41*, 1710-1720.

26. Morton, S. M.; Silverstein, D. W.; Jensen, L. Theoretical Studies of Plasmonics using Electronic Structure Methods. *Chem. Rev.* **2011**, *111*, 3962-3994.

27. Törmä, P.; Barnes, W. L. Strong Coupling Between Surface Plasmon Polaritons and Emitters: A Review. *Rep. Prog. Phys.* **2014**, *78*, 013901/1-34.

28. Yabana, K.; Bertsch, G. F. Time-Dependent Local-Density Approximation in Real Time. *Phys. Rev. B* **1996**, *54*, 4484-4487.

29. Yabana, K.; Nakatsukasa, T.; Iwata, J. I.; Bertsch, G. F. Real-Time, Real-Space Implementation of the Linear Response Time-Dependent Density-Functional Theory. *Phys. Status Solidi (b)* **2006**, *243*, 1121-1138.

30. Baseggio, O.; Fronzoni, G.; Stener, M. A New Time Dependent Density Functional Algorithm for Large Systems and Plasmons in Metal Clusters. *J. Chem. Phys.* **2015**, *143*, 024106/1-12.

31. Castro, A.; Appel, H.; Oliveira, M.; Rozzi, C. A.; Andrade, X.; Lorenzen, F.; Marques, M. A. L.; Gross, E. K. U.; Rubio, A. Octopus: A Tool for the Application of Time-Dependent Density Functional Theory. *Phys. Status Solidi (b)* **2006**, *243*, 2465-2488.

32. Castro, A.; Marques, M. A. L.; Rubio, A. Propagators for the Time-Dependent Kohn–Sham Equations. *J. Chem. Phys.* **2004**, *121*, 3425-3433.

33. Kuisma, M.; Sakko, A.; Rossi, T. P.; Larsen, A. H.; Enkovaara, J.; Lehtovaara, L.; Rantala, T. T. Localized Surface Plasmon Resonance in Silver Nanoparticles: Atomistic First-Principles Time-Dependent Density-Functional Theory Calculations. *Phys. Rev. B* **2015**, *91*, 115431/1-8.

34. Tussupbayev, S.; Govind, N.; Lopata, K.; Cramer, C. J. Comparison of Real-Time and Linear-Response Time-Dependent Density Functional Theories for Molecular Chromophores Ranging from Sparse to High Densities of States. *J. Chem. Theory Comput.* **2015**, *11*, 1102-1109.

35. Weerawardene, K. L. D. M.; Aikens, C. M. Comparison and Convergence of Optical Absorption Spectra of Noble Metal Nanoparticles Computed Using Linear-Response and Real-Time Time-Dependent Density Functional Theories. *Comput. Theor. Chem.* **2018**, *1146*, 27-36.
36. Goings, J. J.; Lestrange, P. J.; Li, X. Real-Time Time-Dependent Electronic Structure Theory. *Wiley Interdiscip. Rev. Comput. Mol. Sci.* **2018**, *8*, e1341/1-19.
37. Baseggio, O.; De Vetta, M.; Fronzoni, G.; Stener, M.; Sementa, L.; Fortunelli, A.; Calzolari, A. Photoabsorption of Icosahedral Noble Metal Clusters: An Efficient TDDFT Approach to Large-Scale Systems. *J. Phys. Chem. C* **2016**, *120*, 12773-12782.
38. Ma, J.; Wang, Z.; Wang, L.-W. Interplay Between Plasmon and Single-Particle Excitations in a Metal Nanocluster. *Nat. Commun.* **2015**, *6*, 10107/1-12.
39. Senanayake, R. D.; Lingerfelt, D. B.; Kuda-Singappulige, G. U.; Li, X.; Aikens, C. M. Real-Time TDDFT Investigation of Optical Absorption in Gold Nanowires. *J. Phys. Chem. C* **2019**, *123*, 14734-14745.
40. Ding, F.; Guidez, E. B.; Aikens, C. M.; Li, X. Quantum Coherent Plasmon in Silver Nanowires: A Real-Time TDDFT Study. *J. Chem. Phys.* **2014**, *140*, 244705/1-7.
41. Townsend, E.; Bryant, G. W. Plasmonic Properties of Metallic Nanoparticles: The Effects of Size Quantization. *Nano Lett.* **2012**, *12*, 429-434.
42. Kadek, M.; Konecny, L.; Gao, B.; Repisky, M.; Ruud, K. X-ray Absorption Resonances Near L2,3-edges from Real-Time Propagation of the Dirac–Kohn–Sham Density Matrix. *Phys. Chem. Chem. Phys.* **2015**, *17*, 22566-22570.
43. Repisky, M.; Konecny, L.; Kadek, M.; Komorovsky, S.; Malkin, O. L.; Malkin, V. G.; Ruud, K. Excitation Energies from Real-Time Propagation of the Four-Component Dirac–Kohn–Sham Equation. *J. Chem. Theory Comput.* **2015**, *11*, 980-991.
44. Bruner, A.; LaMaster, D.; Lopata, K. Accelerated Broadband Spectra Using Transition Dipole Decomposition and Padé Approximants. *J. Chem. Theory Comput.* **2016**, *12*, 3741-3750.
45. Rossi, T. P.; Kuisma, M.; Puska, M. J.; Nieminen, R. M.; Erhart, P. Kohn–Sham Decomposition in Real-Time Time-Dependent Density-Functional Theory: An Efficient Tool for Analyzing Plasmonic Excitations. *J. Chem. Theory Comput.* **2017**, *13*, 4779-4790.

46. Sinha-Roy, R.; García-González, P.; López Lozano, X.; Whetten, R. L.; Weissker, H.-C. Identifying Electronic Modes by Fourier Transform from δ-Kick Time-Evolution TDDFT Calculations. *J. Chem. Theory Comput.* **2018**, *14*, 6417-6426.

47. Rossi, T. P.; Erhart, P.; Kuisma, M. Hot-Carrier Generation in Plasmonic Nanoparticles: Atomic-Scale Structure Matters. *arXiv e-prints* **2020**, arXiv:2002.12087.

48. Yan, L.; Guan, M.; Meng, S. Plasmon-Induced Nonlinear Response of Silver Atomic Chains. *Nanoscale* **2018**, *10*, 8600-8605.

49. Hasan, S. B.; Lederer, F.; Rockstuhl, C. Nonlinear Plasmonic Antennas. *Mater. Today* **2014**, *17*, 478-485.

50. Butet, J.; Brevet, P.-F.; Martin, O. J. F. Optical Second Harmonic Generation in Plasmonic Nanostructures: From Fundamental Principles to Advanced Applications. *ACS Nano* **2015**, *9*, 10545-10562.

51. Krasavin, A. V.; Ginzburg, P.; Zayats, A. V. Free-Electron Optical Nonlinearities in Plasmonic Nanostructures: A Review of the Hydrodynamic Description. *Laser Photonics Rev.* **2018**, *12*, 1700082.

52. Babaze, A.; Esteban, R.; Aizpurua, J.; Borisov, A. G. Second-Harmonic Generation from a Quantum Emitter Coupled to a Metallic Nanoantenna. *ACS Photonics* **2020**, *7*, 701-713.

53. Chauvet, N.; Ethis de Corny, M.; Jeannin, M.; Laurent, G.; Huant, S.; Gacoin, T.; Dantelle, G.; Nogues, G.; Bachelier, G. Hybrid KTP–Plasmonic Nanostructures for Enhanced Nonlinear Optics at the Nanoscale. *ACS Photonics* **2020**, *7*, 665-672.

54. Gürdal, E.; Horneber, A.; Shaqqura, N.; Meixner, A. J.; Kern, D. P.; Zhang, D.; Fleischer, M. Enhancement of the Second Harmonic Signal of Nonlinear Crystals by Self-Assembled Gold Nanoparticles. *J. Chem. Phys.* **2020**, *152*, 104711.

55. Shen, Q.; Jin, W.; Yang, G.; Rodriguez, A. W.; Mikkelsen, M. H. Active Control of Multiple, Simultaneous Nonlinear Optical Processes in Plasmonic Nanogap Cavities. *ACS Photonics* **2020**, *7*, 901-907.

56. Frisch, M. J.; Trucks, G. W.; Schlegel, H. B.; Scuseria, G. E.; Robb, M. A.; Cheeseman, J. R.; Scalmani, G.; Barone, V.; Petersson, G. A.; Nakatsuji, H., et al. *Gaussian Development Version*, Revision I.13+; Gaussian, Inc.: Wallingford CT, 2018.

57. Becke, A. D. Density-Functional Exchange-Energy Approximation with Correct Asymptotic Behavior. *Phys. Rev. A.* **1988**, *38*, 3098-3100.

58. Perdew, J. P. Density-Functional Approximation for the Correlation Energy of the Inhomogeneous Electron Gas. *Phys. Rev. B* **1986**, *33*, 8822-8824.

59. Hay, P. J.; Wadt, W. R. Ab Initio Effective Core Potentials for Molecular Calculations. Potentials for the Transition Metal Atoms Sc to Hg. *J. Chem. Phys.* **1985**, *82*, 270-283.

60. Hay, P. J.; Wadt, W. R. Ab Initio Effective Core Potentials for Molecular Calculations. Potentials for K to Au Including the Outermost Core Orbitals. *J. Chem. Phys.* **1985**, *82*, 299-310.

61. Wadt, W. R.; Hay, P. J. Ab Initio Effective Core Potentials for Molecular Calculations. Potentials for Main Group Elements Na to Bi. *J. Chem. Phys.* **1985**, *82*, 284-298.

62. Harb, M.; Rabilloud, F.; Simon, D.; Rydlo, A.; Lecoultre, S.; Conus, F.; Rodrigues, V.; Félix, C. Optical Absorption of Small Silver Clusters: Ag_n, (n=4–22). *J. Chem. Phys.* **2008**, *129*, 194108.

63. Li, X.; Smith, S. M.; Markevitch, A. N.; Romanov, D. A.; Levis, R. J.; Schlegel, H. B. A Time-Dependent Hartree–Fock Approach for Studying the Electronic Optical Response of Molecules in Intense Fields. *Phys. Chem. Chem. Phys.* **2005**, *7*, 233-239.

64. Lopata, K.; Govind, N. Modeling Fast Electron Dynamics with Real-Time Time-Dependent Density Functional Theory: Application to Small Molecules and Chromophores. *J. Chem. Theory Comput.* **2011**, *7*, 1344-1355.

65. Ding, F.; Van Kuiken, B. E.; Eichinger, B. E.; Li, X. An Efficient Method for Calculating Dynamical Hyperpolarizabilities Using Real-Time Time-Dependent Density Functional Theory. *J. Chem. Phys.* **2013**, *138*, 064104.

66. Walter, M.; Akola, J.; Lopez-Acevedo, O.; Jadzinsky, P. D.; Calero, G.; Ackerson, C. J.; Whetten, R. L.; Grönbeck, H.; Häkkinen, H. A Unified View of Ligand-Protected Gold Clusters as Superatom Complexes. *Proc. Natl. Acad. Sci. U.S.A.* **2008**, *105*, 9157-9162.

67. Raghunathan, S.; Nest, M. The Lack of Resonance Problem in Coherent Control with Real-Time Time-Dependent Density Functional Theory. *J. Chem. Theory Comput.* **2012**, *8*, 806-809.

68. Provorse, M. R.; Habenicht, B. F.; Isborn, C. M. Peak-Shifting in Real-Time Time-Dependent Density Functional Theory. *J. Chem. Theory Comput.* **2015**, *11*, 4791-4802.

69. Luo, K.; Fuks, J. I.; Maitra, N. T. Studies of Spuriously Shifting Resonances in Time-Dependent Density Functional Theory. *J. Chem. Phys.* **2016**, *145*, 044101.

70. Provorse, M. R.; Isborn, C. M. Electron Dynamics with Real-Time Time-Dependent Density Functional Theory. *Int. J. Quantum Chem.* **2016**, *116*, 739-749.

71. Göppert-Mayer, M. Über Elementarakte mit zwei Quantensprüngen. *Ann. Phys. (Berl.)* **1931**, *401*, 273-294.

72. McClain, W. M. Two-Photon Molecular Spectroscopy. *Acc. Chem. Res.* **1974**, *7*, 129-135.

73. Wirth, M. J.; Koskelo, A.; Sanders, M. J. Molecular Symmetry and Two-Photon Spectroscopy. *Appl. Spectrosc.* **1981**, *35*, 14-21.

74. McClain, W. M. Excited State Symmetry Assignment Through Polarized Two-Photon Absorption Studies of Fluids. *J. Chem. Phys.* **1971**, *55*, 2789-2796.

TOC Graphic